















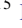




Anti-Solar Differential Rotation May Have Revived Magnetic Braking in the Subgiant 31 Aquilae

TRAVIS S. METCALFE ¹, JENNIFER L. VAN SADERS ², THOMAS R. AYRES ³, DEREK BUZASI ⁴, JEREMY J. DRAKE ⁵,
RICKY EGELAND ¹, RAFAEL A. GARCÍA ⁶, OLEG KOCHUKHOV ⁷, STEVEN H. SAAR ⁸, KEIVAN G. STASSUN ⁹,
SARBANI BASU ¹⁰, J. M. JOEL ONG ¹¹, AMALIE STOKHOLM ¹², TIMOTHY R. BEDDING ¹¹, SYLVAIN N. BRETON ¹³,
ILYA V. ILYIN ¹⁴, PASCAL PETIT ¹⁵, MARC H. PINSONNEAULT ¹⁶ AND KLAUS G. STRASSMEIER ¹⁴

¹Center for Solar-Stellar Connections, WDRC, 9020 Brumm Trail, Golden, CO 80403, USA

²Institute for Astronomy, University of Hawai'i, 2680 Woodlawn Drive, Honolulu, HI 96822, USA

³Center for Astrophysics and Space Astronomy, 389 UCB, University of Colorado, Boulder, CO 80309, USA

⁴Department of Astronomy & Astrophysics, University of Chicago, 5640 S. Ellis Avenue, Chicago, IL 60637, USA

⁵Lockheed Martin Solar and Astrophysics Laboratory, 3251 Hanover St, Palo Alto, CA 94304, USA

⁶Université Paris-Saclay, Université Paris Cité, CEA, CNRS, AIM, 91191, Gif-sur-Yvette, France

⁷Department of Physics and Astronomy, Uppsala University, Box 516, SE-75120 Uppsala, Sweden

⁸Harvard-Smithsonian Center for Astrophysics, Cambridge, MA 02138, USA

⁹Vanderbilt University, Department of Physics & Astronomy, 6301 Stevenson Center Lane, Nashville, TN 37235, USA

¹⁰Department of Astronomy, Yale University, PO Box 208101, New Haven, CT 06520-8101, USA

¹¹Sydney Institute for Astronomy (SIfA), School of Physics, University of Sydney, Camperdown, NSW 2006, Australia

¹²School of Physics & Astronomy, University of Birmingham, Edgbaston, Birmingham B15 2TT, UK

¹³INAF – Osservatorio Astrofisico di Catania, Via S. Sofia, 78, 95123 Catania, Italy

¹⁴Leibniz-Institut für Astrophysik Potsdam (AIP), An der Sternwarte 16, D-14482 Potsdam, Germany

¹⁵Université de Toulouse, CNRS, CNES, 14 avenue Edouard Belin, 31400, Toulouse, France

¹⁶Department of Astronomy, The Ohio State University, 140 West 18th Avenue, Columbus, OH 43210, USA

ABSTRACT

Recent observations have shown that sufficiently slow rotation disrupts the organization of large-scale magnetic field in older main-sequence stars, leading to weakened magnetic braking (WMB) and the collapse of the global stellar dynamo. Recent simulations predict a shift from solar-like to anti-solar differential rotation (DR) at slower rotation rates, which typically do not occur on the main-sequence due to WMB. However, physical expansion on the subgiant branch can eventually slow the stellar rotation beyond this threshold, yielding a non-cycling large-scale field that revives magnetic braking. We combine asteroseismology from the Transiting Exoplanet Survey Satellite (TESS) with spectropolarimetry from the Large Binocular Telescope (LBT) to test these predictions in the old metal-rich subgiant 31 Aql. The LBT observations reveal a strong large-scale magnetic field in this star, and archival measurements of its chromospheric emission over 50 years confirm that it is non-cycling, as predicted. The star exhibits a variety of rotation periods during different observing seasons, consistent with DR but with no means of distinguishing between solar-like and anti-solar patterns. We incorporate the TESS observations to estimate the current wind braking torque of 31 Aql, demonstrating that it supports revived magnetic braking in this old subgiant. We also use rotational evolution modeling to place a preliminary constraint on the stellar Rossby number for the transition to anti-solar DR. Future refinements in both asteroseismic observations and rotational modeling may yield improvements to this initial analysis.

1. INTRODUCTION

The influence of stellar rotation on global convective patterns changes dramatically throughout the lives of solar-type stars. In the earliest phases of stellar evolution, rapid rotation imprints a cylindrical pattern of differential rotation (DR) on the surface convection zone, with a fast equator and slower poles in a configuration known as the Taylor-Proudman state (Proudman 1916; Taylor 1917). As the magnetized stellar wind gradually sheds angular momentum, rotation slows and the DR pattern becomes more conical as observed in the Sun

(Thompson et al. 1996), with contours of constant rotation extending almost radially through the convection zone rather than parallel to the rotation axis. When the rotation rate becomes comparable to the convective overturn timescale (τ_c), a broad array of convection simulations suggest that the DR pattern will flip from solar-like to anti-solar, with a slow equator and faster poles (Gastine et al. 2014). However, observational confirmation of anti-solar DR has been mostly confined to red giant stars (Weber et al. 2005).

Our understanding of stellar rotational evolution has been updated substantially over the past decade, modifying our expectations for the detection of anti-solar DR. After stars contract onto the main-sequence and magnetic braking begins to dominate their rotational evolution, the empirical relations of Skumanich (1972) approximate the decline of stellar activity and the gradual slowing of rotation with the square-root of stellar age. The discovery of weakened magnetic braking (WMB) in old Kepler field stars was the first indication that this orderly progression does not continue indefinitely, but is disrupted at activity levels close to solar (van Saders et al. 2016; Metcalfe et al. 2016). Observational constraints on the large-scale magnetic field strength and the mass-loss rates of older stars revealed unexpected changes in both properties that combine to produce WMB and keep stellar rotation nearly constant during the second half of main-sequence lifetimes (Metcalfe et al. 2025). Consequently, stars may not reach the slow rotation rates that are required for the shift to anti-solar DR until the physical expansion associated with core H exhaustion finally pushes them over this threshold.

Recent simulations predict some observational signatures that accompany the shift from solar-like to anti-solar DR, including the emergence of a non-cycling large-scale magnetic field. A set of dynamo simulations described by Brun et al. (2022) show a gradual transition from short activity cycles for rapidly rotating models to longer sun-like cycles for intermediate rotation near the solar rate, and no cycles for models rotating more slowly than the Sun. Similar results were reported by Strugarek et al. (2017) for a completely independent set of dynamo simulations, and both sets of models lend qualitative support to the evolutionary scenario proposed by Metcalfe & van Saders (2017). The simulations also show a gradual decline in the large-scale magnetic field strength as activity cycles grow longer, reaching a minimum near the solar rotation rate and increasing once again for more slowly rotating models with no cycles and anti-solar DR (Noraz et al. 2024). These results suggest that stars with anti-solar DR might be expected to show approximately constant activity from a stationary large-scale magnetic field. Crucially, the rotation rates that are required to produce anti-solar DR in the simulations are slower than FGK stars can typically reach on the main-sequence under the influence of WMB.

The metal-rich G7 subgiant 31 Aql (b Aql, HD 182572, TIC 359981217) may have already evolved through the transition to anti-solar DR. In more than 50 years of chromospheric activity monitoring from the Mount Wilson survey (Baliunas et al. 1995) and the Keck observatory (Baum et al. 2022), 31 Aql shows minimal long-term variability around a low average activity level ($\log R'_{\text{HK}} = -5.1$), while the short-term variability is sufficient to measure a rotation period of $P_{\text{rot}} \sim 41$ days (Baliunas et al. 1996). The latter suggests a Rossby number ($\text{Ro} \equiv P_{\text{rot}}/\tau_c$) that may be well above the

solar value, potentially in the realm of anti-solar DR. In Section 2 we analyze new and archival observations to characterize 31 Aql, including time series photometry from the Transiting Exoplanet Survey Satellite (TESS; Ricker et al. 2014), spectropolarimetry from the Large Binocular Telescope (LBT), X-ray measurements from Chandra, and ultraviolet observations from Hubble. In Section 3 we use these observations to determine precise stellar properties from asteroseismology, and to constrain the evolutionary pathway that led to the current magnetic and rotational configuration. Finally, in Section 4 we discuss our results and compare them to the predictions of dynamo simulations, to assess the possibility that 31 Aql might exhibit anti-solar DR.

2. OBSERVATIONS

Below we analyze new and archival observations of 31 Aql to characterize the stellar properties that are relevant to its magnetic and rotational evolution. In Section 2.1 we identify solar-like oscillation frequencies from recent TESS photometry. In Section 2.2 we analyze new LBT spectropolarimetry to estimate the large-scale magnetic field strength, and we verify its persistence in archival observations. In Section 2.3 we use recent X-ray measurements from Chandra to estimate the mass-loss rate, and in Section 2.4 we present new ultraviolet observations from Hubble. In Section 2.5 we use archival Mount Wilson data to confirm the absence of an obvious activity cycle and to extract seasonal rotation measurements. Finally, in Section 2.6 we determine the bolometric luminosity from the spectral energy distribution (SED).

2.1. TESS Photometry

TESS observed 31 Aql at 120 s cadence during Sector 54 (2022 July 9 – 2022 August 5) and at 20 s cadence during Sector 81 (2024 July 15 – 2024 August 10). In this analysis we use only the Sector 81 data because the 20 s cadence has lower noise than 120 s cadence data for bright stars (Huber et al. 2022). We extracted the data from the raw image frames following the process described in Nielsen et al. (2020) and Metcalfe et al. (2023b), which uses aperture masks optimized to produce the highest signal-to-noise (S/N) ratio possible with simple aperture photometry on an isolated star; in this case our mask contained 85 pixels from the 297-pixel postage stamp. Conservatively, we discarded observations with flag values greater than unity, leaving 106,244 data points with a duty cycle above 92%. Finally, we detrended the light curve against centroid pixel coordinates, breaking the time series into two parts separated by the data downlink gap starting near day 3519. The resulting light curve has a noise level that is approximately 11% lower compared to the Science Processing Operations Center (SPOC; Jenkins et al. 2016) PDCSAP product. Prior to frequency analysis, the light curve was gap filled using a multi-scale discrete cosine transform following inpainting principles (García et al.

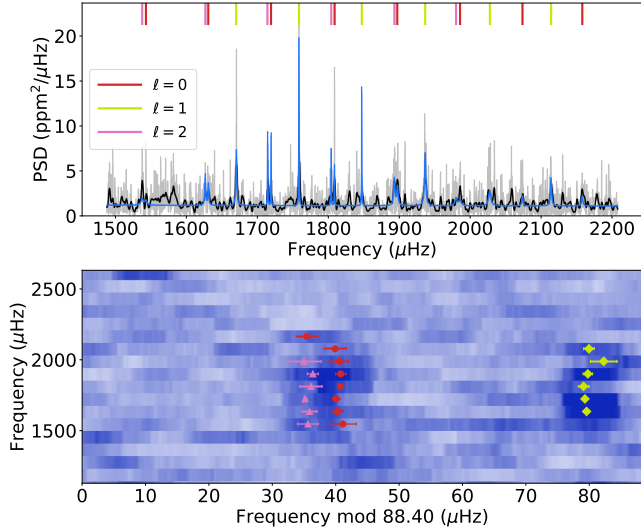


Figure 1. *Top:* Power spectral density (PSD) in the frequency range of the fitted modes. In gray is the raw spectrum and in black a smoothed PSD. The blue line represents the fitted spectrum. The vertical red, yellow, and magenta bars indicate the central frequencies of the $\ell = 0$, 1, and 2 modes, respectively. *Bottom:* Échelle diagram with $\Delta\nu = 88.40 \mu\text{Hz}$. The fitted modes and their associated uncertainties are shown as circles, diamonds, and triangles with the same color code as in the top panel.

2014; Pires et al. 2015), and high-pass filtered with a cut-off frequency of $100 \mu\text{Hz}$ to minimize residual contributions from spacecraft jitter. The power spectrum of this light curve is illustrated in the top panel of Figure 1, with an échelle diagram in the bottom panel to facilitate the identification of the spherical harmonic degree (ℓ) for each frequency.

The solar-like oscillation frequencies were identified using the `apollinaire`¹ code (Breton et al. 2022), which is built upon the `emcee` ensemble Markov Chain Monte Carlo sampler (Foreman-Mackey et al. 2013). In this framework, each mode is described by a Lorentzian function, where both the central frequency and the linewidth are treated as independent parameters. Rather than fitting an individual height for each mode, a single height parameter is assigned “by order n ”, i.e., to all modes with $\ell = 0, 1$ at a given radial order n , and to $\ell = 2$ modes at order $n - 1$. The ratios of mode heights between different angular degrees are incorporated as global parameters. The free parameters for all modes were fit simultaneously in a global procedure, following the methodology pioneered by Roca Cortés et al. (1999) and improved by Fletcher et al. (2008), which helps to account for correlations between modes and provides a more robust estimation of the oscillation parameters. The identified oscillation frequencies and their uncertainties are listed in Table 1 and shown in

¹ Documentation is available at <https://apollinaire.readthedocs.io/>.

Table 1. Identified Oscillation Frequencies for 31 Aql

n	ℓ	ν (μHz)	σ_ν (μHz)
17	0	1543.92	2.09
18	0	1631.51	0.91
19	0	1719.66	0.57
20	0	1808.74	0.20
21	0	1897.20	0.81
22	0	1985.40	1.39
23	0	2073.11	1.75
24	0*	2157.08	1.71
18	1	1670.78	0.38
19	1	1758.92	0.17
20	1	1847.10	0.83
21	1	1936.18	0.75
22	1	2027.08	2.08
23	1	2113.15	0.83
16	2	1538.43	1.65
17	2	1627.07	1.16
18	2	1714.77	0.28
19	2	1804.10	1.74
20	2	1892.79	0.87
21	2	1979.80	2.67

NOTE—* Possible misidentification of an ($n = 23$, $\ell = 2$) mode.

Figure 1. Posterior probability distributions were generated for each parameter, and the median of each distribution was adopted as the central value. The adopted uncertainties are the average of the differences between the median and the 16th and 84th percentiles of the posterior distributions.

2.2. Spectropolarimetry

We observed 31 Aql with the Potsdam Echelle Polarimetric and Spectroscopic Instrument (PEPSI; Strassmeier et al. 2015) installed at the $2 \times 8.4 \text{ m}$ LBT. The observation comprised a single snapshot taken on 2025 July 6. We employed the same instrumental setup (spectral resolution $R = 130,000$ with wavelength coverage spanning the 475–540 and 623–743 nm regions) and data reduction procedures as described in Metcalfe et al. (2019). Given the low expected amplitude of the polarization signal, we applied the least-squares deconvolution (LSD; Donati et al. 1997; Kochukhov et al. 2010) technique to extract high S/N mean intensity and circular polarization profiles.

The line mask required for LSD was obtained from the Vienna Atomic Line Database (VALD; Ryabchikova et al. 2015), with atmospheric parameters $T_{\text{eff}} = 5500 \text{ K}$, $\log g = 4.0$, and metallicity $[M/H] = +0.3$, comparable to Brewer et al. (2016). For the analysis of the PEPSI observation, we used

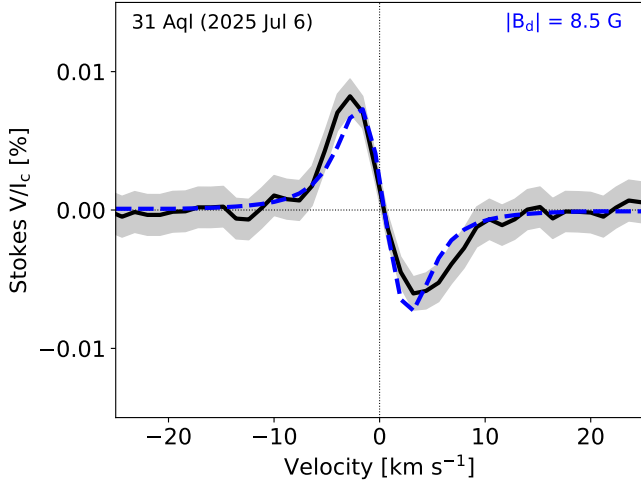


Figure 2. Stokes V polarization profile for 31 Aql from LBT observations on 2025 July 6. The observed LSD profile is shown as a black line, with uncertainties indicated by the gray shaded area. The dashed blue line is a model profile assuming an axisymmetric dipole morphology with a fixed inclination.

2568 metal lines deeper than 10% of the continuum. The LSD procedure yielded a polarization profile with a precision of 4.18 ppm and a clear detection of the stellar magnetic field, as illustrated in Figure 2. The Stokes V signature of 31 Aql corresponds to a mean longitudinal magnetic field $\langle B_z \rangle = 1.525 \pm 0.053$ G. We subsequently estimated the strength of an axisymmetric dipole magnetic field using the modeling procedure described in Metcalfe et al. (2019), fixing the inclination angle at $i = 61^\circ$ (Bowler et al. 2023). This analysis yielded a dipole field strength of $B_d = 8.5 \pm 1.1$ G.

We complemented the PEPSI observation of 31 Aql with an analysis of archival spectropolarimetric data retrieved from PolarBase (Petit et al. 2014). This database includes two ESPaDOnS observations of 31 Aql obtained in 2007, as well as 15 NARVAL Stokes V spectra acquired over three nights in 2019. Both spectropolarimeters cover the 370–1000 nm wavelength range at a spectral resolution of $R = 65,000$. All spectra were processed using the same LSD procedure described above, but employing a line mask consisting of 5,306 spectral lines deeper than 20% of the continuum.

Among the 15 NARVAL observations, a definite Zeeman signature indicative of a positive global magnetic field was detected in every spectrum, whereas the two earlier ESPaDOnS observations yielded no detection owing to their lower S/N ratios. The LSD Stokes V profiles of 31 Aql obtained from NARVAL observations exhibit amplitudes of order $\sim 10^{-4}$ of the continuum, similar to the LSD profile derived from the PEPSI spectrum, enabling measurements of the mean longitudinal magnetic field in the range of 1–2 G with typical uncertainties of 0.3 G. The circular polarization signal appears stable, with no significant variability detected between nights. To further quantify the strength of the large-

scale magnetic field in these archival spectra of 31 Aql, we selected the five NARVAL observations with the highest S/N ratios and applied the axisymmetric dipole fitting methodology described above. This analysis yielded an average dipole field strength of $B_d = 7.9 \pm 0.7$ G, where the quoted uncertainty corresponds to the standard deviation of the fitting results for the individual spectra. Thus, the NARVAL measurements were consistent with those from PEPSI.

2.3. X-Ray Measurements

The subgiant 31 Aql was captured in the ROSAT All-Sky survey in 1990 October as a faint source in 0.50 ks of accumulated exposure. The count rate was 0.029 ± 0.009 counts s^{-1} (0.1–2.4 keV) as reported in the rassfsc catalog (released circa 2000), and 0.037 ± 0.011 counts s^{-1} in the updated rass2rxs (circa 2016). More recently, in 2019 November, Chandra carried out a 9 ks pointing on 31 Aql with the High-Resolution Camera (HRC-I: ObsID 22309; PI: T. Metcalfe). Although HRC-I lacks any meaningful energy resolution, it was the only viable option for the soft coronal source 31 Aql—the other Chandra camera (ACIS) is affected by an ongoing organic contamination issue that severely reduces the sensitivity to low-energy photons. Further, there were no observations of 31 Aql listed in the archives of the other main contemporary high-energy facilities: XMM-Newton and the Swift X-ray Telescope.

Figure 3 is a photon map, in relative sky coordinates, of the center of the HRC-I field, showing a prominent point source within $0''.4$ of the predicted location of the bright star in that epoch (typical of the accuracy of the Chandra aspect solution). There are no other significant X-ray point sources in the $50'' \times 50''$ field. The small red circle indicates the adopted $3''$ -diameter detection cell (95% encircled energy). The Washington Double Star Catalog reports a faint visual component “E” to 31 Aql (WDS J19250+1157A) in 2002 at position angle 288° , separation of $4''.2$, and a magnitude deficit of ≈ 7 in the K-band. However, Gaia DR3 (epoch 2015.5) lists no entries within $30''$ of the nearby subgiant, brighter than $G = 17$ or with a parallax greater than 1 mas, so component E must be a background object not sharing the high proper motion of 31 Aql.

The 31 Aql HRC-I level 2 event list from the Chandra Archive was processed as described by Ayres (2025). The gross number of counts in the $3''$ -diameter detection cell was 89 ± 9.4 in the 8.99 ks of dead-time corrected exposure. The background was sampled in an annulus $50''$ – $60''$ from the source, resulting in an areal rate of 3.9×10^{-5} counts $('')^{-2} s^{-1}$, typical of HRC-I pointings. This implied a background contribution scaled to the detection cell of 2.5 counts. The net HRC-I count rate, corrected for the encircled energy factor, was 0.0101 ± 0.0011 counts s^{-1} . As shown in Figure 3, there was no obvious variability of the source (e.g., flare activity)

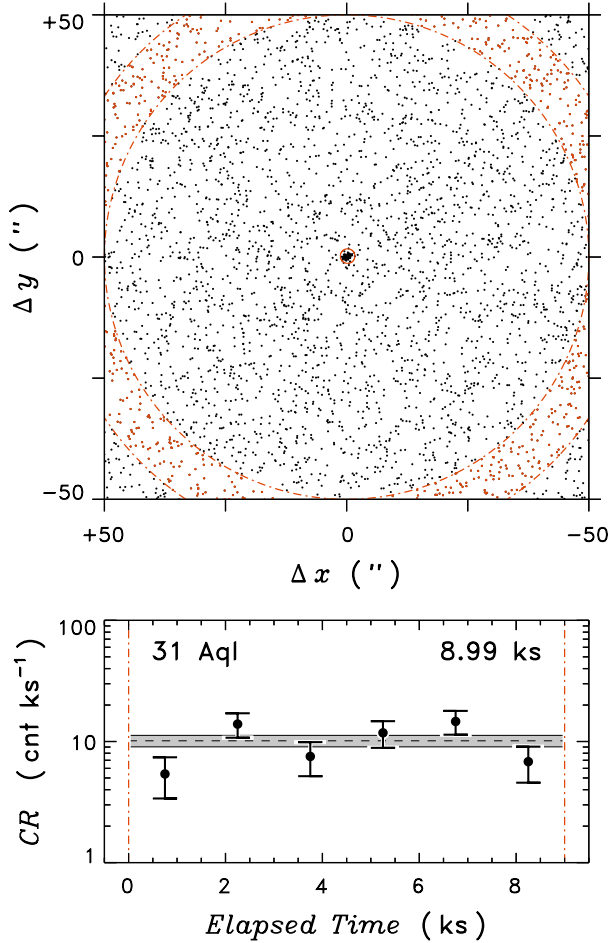


Figure 3. *Top:* Photon map derived from the 2019 Chandra HRC-I pointing on 31 Aql. The axes are sky coordinates relative to the source centroid. The small red circle is the $3''$ detection cell; the outer red circles, and red dots, delimit the background extraction zone. *Bottom:* Time-binned X-ray count rates ($\Delta t = 1500$ s) from the HRC-I pointing, corrected for background and the encircled energy fraction, as a function of elapsed time (the dead-time corrected exposure was 8.99 ks). The gray band indicates the average count rate and $\pm 1 \sigma$ Poisson uncertainty for the full observation.

when the event list was blocked into multiple time segments (six was the maximum given the low count rate).

The ROSAT/PSPC and Chandra/HRC-I count rates were then calibrated into flux units by calculating optimum energy conversion factors (ECF) for the two instrument configurations based on a grid of coronal emission-measure models (see Ayres 2025, for details). An apparent slow systematic decline of the HRC-I sensitivity since 2016 was taken into account. The ECF optimization made use of the adopted fundamental parameters of 31 Aql, namely $T_{\text{eff}} = 5587$ K and $f_{\text{bol}} = 2.24 \times 10^{-7}$ erg s $^{-1}$ cm $^{-2}$, and a hydrogen column density to the nearby star ($d = 14.92$ pc) of $N_{\text{H}} = 1 \times 10^{18}$ cm $^{-2}$.

The ROSAT rass2rxs count rate yielded an X-ray luminosity $L_{\text{X}} = (4.5 \pm 1.3) \times 10^{27}$ erg s $^{-1}$, while the Chandra HRC-I result was somewhat lower, $L_{\text{X}} = (2.4 \pm 0.3) \times 10^{27}$ erg s $^{-1}$. The HRC-I luminosity is consistent with the less certain rass2rxs value, within the typical ranges of short-term and long-term variability seen in normal stars (Ayres 2025). We adopt the higher-quality HRC-I X-ray luminosity, recognizing that a factor of two uncertainty would not be unusual. However, as noted in Section 2.5, the chromospheric activity level of the star has been relatively flat in recent years, especially during the epoch of the HRC-I pointing.

We can estimate the mass-loss rate of 31 Aql by combining the adopted X-ray luminosity with the stellar radius determined from asteroseismology (see Section 3.1). For stars with mass-loss rates inferred directly from observations of Ly α , there is an empirical relation between the mass-loss rate and the X-ray flux per unit surface area, $\dot{M} \propto F_{\text{X}}^{1.29 \pm 0.16}$ (Wood 2018). The resulting estimate is slightly above the solar value, $\dot{M} = 1.05^{+1.08}_{-0.58} \dot{M}_{\odot}$. The uncertainty accounts for the errors on L_{X} , R and the power law exponent combined in quadrature with a factor of 2 systematic uncertainty on the empirical relation (Wood et al. 2005).

2.4. Hubble Space Telescope Data

As a probe of the physical environment between the photosphere and the corona, we also observed 31 Aql using the Cosmic Origins Spectrograph (COS) on the Hubble Space Telescope (HST). The description below closely follows a similar analysis of λ Ser by Metcalfe et al. (2023b). We obtained a low resolution G140L FUV spectrum with an integration time of ≈ 1940 s on 2020 March 2 (program 15991), which was reduced with standard pipeline processing. We computed integrated fluxes for isolated emission lines in the rest frame of the star above nearby pseudo-continua, together with root-mean-square (RMS) errors. We estimated continua from linear fits to clusters of low points on either side of the line in question. When the target line was blended, two methods were employed. Some weaker blends were removed by fitting a Voigt function to better mimic the convolved instrumental profile and line shape, leaving the residual target line for flux integration as before. In some cases, we fit the entire complex of lines with multiple Voigt functions. The results are listed in Table 2. Tests on isolated lines demonstrated that straight integration and Voigt fitting yielded similar results, typically within $\pm 5\%$. In several cases, multiple nearby lines of the same ion were combined. Following Ayres (2020), we also measured a 10 Å segment of relatively line-free FUV pseudo-continuum centered at 1506 Å.

We can compare the FUV fluxes of 31 Aql to the Sun (Ayres 2020) and to λ Ser (Metcalfe et al. 2023b), a somewhat hotter solar analog (see Table 3). With the exception of the hottest lines, 31 Aql generally shows surface fluxes quite

Table 2. Measured FUV Line Fluxes for 31 Aql

Ion(s)	Wavelength	Flux at Earth
	[Å]	[10^{-15} ergs cm $^{-2}$ s $^{-1}$]
C III ¹	1175	10.1 ± 1.3
O I ¹	1304	55.4 ± 1.1
C II ¹	1335	30.5 ± 0.9
Cl I ²	1351.7	1.1 ± 0.3
O V	1371	0.21 ± 0.1
Si IV	1393.8	8.0 ± 0.7
O IV	1399.8	0.10 ± 0.3
O IV	1401.2	0.48 ± 0.3
Si IV ²	1402.8	5.5 ± 0.6
Si IV+O IV ²	1404.8	0.24 ± 0.6
O IV ²	1407.4	0.21 ± 0.16
Continuum ³	1506	3.7 ± 0.8
Si II	1526.5	1.6 ± 0.9
Si II	1533.7	2.4 ± 0.8
C IV ²	1548	15.3 ± 1.3
C IV ²	1550	7.7 ± 1.1
C I ^{1,2}	1561	8.6 ± 1.0
He II	1640.7	6.2 ± 1.5
C I ¹	1657	29.9 ± 2.5
O III	1666.2	1.7 ± 1.2
Si II	1808.0	22.4 ± 3.1
Si II	1817.1	61.6 ± 5
Al III	1854.6	7.1 ± 3.6
Si III	1892.0	20.6 ± 6.6
C III	1908.7	11.8 ± 7.9

NOTE—All fluxes are from direct integration, except ¹Multiple lines combined, ²Voigt function fitting and deblending, ³±5 Å integration of a largely line-free region.

similar to the Sun. Lower chromospheric surface flux in Cl I (with temperatures of peak emissivity $\log T_{\text{peak}} = 3.8$) is 1.3 times smaller than λ Ser; the upper chromospheric C II flux ($\log T_{\text{peak}} = 4.5$) is similarly $\approx 1.5\times$ reduced. In hotter lines formed in the stellar transition region, C III ($\log T_{\text{peak}} = 4.8$) is $\approx 1.9\times$ weaker relative to λ Ser, Si IV ($\log T_{\text{peak}} = 4.9$) is similarly reduced. In the C IV doublet ($\log T_{\text{peak}} = 5.0$), fluxes are somewhat stronger—a factor of ≈ 1.7 lower than λ Ser, and 10% weaker than the solar value (here some optical depth effects may play a role).

A number of density-sensitive line ratios can be found in the HST spectra. We use a combination of these results to estimate the electron density in the stellar transition region. The ratio C III(1908 Å)/Si IV(1402 Å), with $\log T_{\text{peak}} \sim 4.8$, gives $\log n_e = 9.98^{+0.05}_{-0.06}$. The Si III(1892 Å)/C III(1909 Å) ratio, with $\log T_{\text{peak}} \sim 4.7$, yields $\log n_e = 9.87^{+0.08}_{-0.18}$ using Keenan et al. (1987). The ratios O III(1666 Å)/Si IV(1402 Å) and

Table 3. Comparison of FUV Surface Fluxes

Ion(s)	Wavelength	Surface Flux [10^3 ergs cm $^{-2}$ s $^{-1}$]		
		31 Aql	λ Ser	Sun ²
C III ¹	1175	2290	4400	2250
O I ¹	1304	12600	8230	5490
C II ¹	1335	6940	10700	7000
Cl I	1351.7	245	330	252
Si IV	1393.8	1830	4110	1690
Si IV	1402.8	1260	1870	875
Continuum	1506	830	3210	1780
C IV	1548	3490	6030	3800
C IV	1550	1760	2730	1960

NOTE—¹Multiple lines combined, ²Results from Ayres (2020).

C III(1908 Å)/O III(1666 Å), also with $\log T_{\text{peak}} \sim 4.8$, were less certain, affected by larger errors in the O III line; these yield $\log n_e = 10.80^{+0.40}_{-0.41}$ and $9.76^{+0.30}_{-1.44}$, respectively (using Keenan et al. 1988). Combining the diagnostics, we find an average $\langle \log n_e \rangle = 9.95 \pm 0.05$ at $\log T_{\text{peak}} \sim 4.8$. For comparison, $\langle \log n_e \rangle = 10.0$ using the hotter O IV ratio in the Sun (e.g., Rao et al. 2022). This suggests that 31 Aql has transition region densities similar to, or perhaps slightly lower than, the Sun at fixed temperature, which is consistent with its lower surface gravity. We caution, however, that assumptions intrinsic to the line ratio method make the results uncertain (see discussion in Judge et al. 2020).

In summary, 31 Aql has chromospheric and transition region fluxes broadly consistent with a star which has similar coronal activity, and has slightly lower density than the Sun. It is also a factor of ~ 1.3 – 2 less active than the evolved solar analog λ Ser, with larger reductions towards hotter lines.

2.5. Chromospheric Activity Data

The Mount Wilson Observatory (MWO) HK Project (Wilson 1978; Baliunas et al. 1995) defined the S -index of chromospheric activity based on the core of the Ca II H & K emission lines relative to nearby pseudo-continuum bands (Vaughan et al. 1978). Baum et al. (2022) combined these data with observations from Keck HIRES, and the composite time series is shown in Figure 4. The combined time series shows more than 50 years of relatively flat activity punctuated by a few periods of enhanced activity. Observations are sparse from 1966–1982, as well as during the Keck time series, but the period from 1982 through 2001 has a sufficient number of observations per season to attempt to measure a seasonal rotation period. As described in Donahue et al. (1996), the range of seasonal rotation periods is presumed

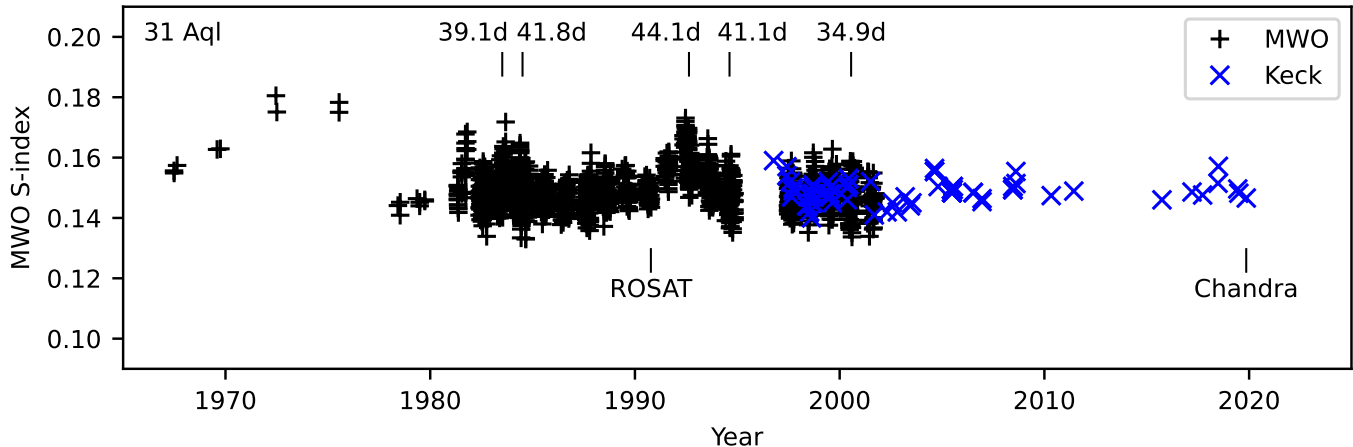


Figure 4. Chromospheric activity measurements of 31 Aql spanning more than 50 years from Mount Wilson (black plus) and Keck (blue cross), showing minimal long-term variability but sufficient short-term variability to measure the rotation period. Data are from [Baum et al. \(2022\)](#).

to be due to surface features (spots or faculae) transiting the star at different rates due to DR.

Using the methods described in [Metcalf et al. \(2023b\)](#) we analyzed 14 out of 24 MWO seasons with $N \geq 20$ observations using the Lomb-Scargle periodogram in a Monte Carlo fashion to estimate the seasonal rotation period, false alarm probability (FAP), and uncertainty in period. We detected significant seasonal rotation periods (FAP < 5%; 95% confidence) in 6 out of 14 seasons. The results are shown in Table 4, along with the seasonal mean S -index. Five of the six significant periods were detected near times of high activity; there are local maxima in the seasonal mean time series in 1983, 1989, 1992, and 1999. This is to be expected as the S -index is enhanced by the presence of magnetic regions on the surface, and larger magnetic regions at activity maximum would produce a stronger rotational modulation of the S -index. The significant rotation signals ranged from 34.9 to 44.1 days, with one outlier (FAP = 3.3%) at 15.1 days in the 1985 season. We reject this period based on the expectation of less extreme DR from observations of the Sun and other stellar analyses ([Donahue et al. 1996](#)). Indeed, with our threshold of FAP < 5% we expect a spurious detection in 1 of 20 seasons, on average, with the FAP defined as the probability of pure noise producing a peak above the selected

power threshold. Excluding the 1985 season and taking the error-weighted mean of the remaining seasonal periods, we find a mean rotation period of $P_{\text{rot}} = 40.3 \pm 1.5$ days, where the uncertainty is the error in the mean, σ/\sqrt{N} .

The range of the seasonal rotation periods $\Delta P = P_{\text{max}} - P_{\text{min}}$ is 9.2 days. This compares well to the work of [Donahue et al. \(1996\)](#) who found a power law relationship $\Delta P \propto P^{1.3 \pm 0.1}$ for an ensemble of stars in the MWO survey. Donahue did not publish the proportionality constant, but using their data for the Sun ($P_{\text{rot}} = 26.09$ days, $\Delta P = 4.0$ days), we find it to be $C = 0.0576$. Finally, using $\Delta P_{\text{D96}} = CP^{1.3}$ with our mean rotation period we obtain the empirical range of 7.0 days, comparable to our measured value of 9.2 days. This provides additional confidence that we found a reasonable spread in rotation periods that resembles DR. It is likely a lower limit on the magnitude of DR, as magnetic features are not expected to appear at all latitudes.

[Donahue \(1993\)](#) further examined stellar DR by constructing an “active region migration diagram” consisting of seasonal P_{rot} versus mean seasonal activity $\langle S \rangle$. For the Sun, this produces a wedge-like diagram as the solar cycle begins with low activity and long rotation period with spots emerging at the highest latitudes, proceeds to high-activity solar maximum with mid-latitude spots and medium rotation period, and finishes with low activity again and fast rotation as spots appear near the equator. Donahue proposed that if we assume solar-like active region migration from high to low latitudes (an unsupported assumption) then anti-solar DR would manifest as a similar wedge-like pattern in opposite time order. Donahue identified several candidates for anti-solar DR using this technique. We attempted to apply this technique to our data for 31 Aql, but there are not enough sequential seasonal rotation measurements and the activity does not have sufficiently long rise/decline phases to apply the method. Therefore, while we find that 31 Aql has a range

Table 4. Seasonal Measurements from the MWO Data

Season	N	$\langle S \rangle$	P_{rot} (days)	FAP (%)
1983	69	0.1523 ± 0.0050	39.1 ± 0.6	0.0056
1984	75	0.1499 ± 0.0006	41.8 ± 0.4	0.0006
1992	36	0.1599 ± 0.0010	44.1 ± 0.5	0.0556
1994	45	0.1486 ± 0.0006	41.1 ± 3.0	2.3
2000	25	0.1482 ± 0.0012	34.9 ± 0.5	2.6

of seasonal rotation periods consistent with DR, we cannot determine whether it follows a solar-like or anti-solar pattern from the rotation and activity data alone.

2.6. Spectral Energy Distribution

To obtain a luminosity constraint for asteroseismic modeling, we performed an analysis of the broadband SED of 31 Aql together with the Gaia DR3 parallax (with no systematic offset applied; see, e.g., [Stassun & Torres 2021](#)), following the procedures described in [Stassun & Torres \(2016\)](#) and [Stassun et al. \(2017, 2018\)](#). We obtained the JHK_S magnitudes from *2MASS*, the *UBV* magnitudes from the homogeneous photometric catalog of [Mermilliod \(2006\)](#), and the Strömgren *uvby* magnitudes from [Paunzen \(2015\)](#). Together, the available photometry spans the full optical-IR stellar SED over the wavelength range 0.3–2 μm .

We performed a fit using Kurucz stellar atmosphere models, with the effective temperature T_{eff} , surface gravity $\log g$, and the metallicity $[M/H]$ adopted from [Brewer et al. \(2016\)](#). The extinction A_V was set to zero based on the proximity of the system. The resulting fit has a reduced $\chi^2 = 1.2$. Integrating the model SED gives the bolometric flux at Earth, $f_{\text{bol}} = 2.243 \pm 0.079 \times 10^{-7} \text{ erg s}^{-1} \text{ cm}^{-2}$. Taking the f_{bol} together with the Gaia parallax directly yields the bolometric luminosity, $L_{\text{bol}} = 1.557 \pm 0.055 L_{\odot}$. The stellar radius follows from the Stefan-Boltzmann relation, giving $R = 1.333 \pm 0.024 R_{\odot}$. In addition, we can estimate the stellar mass from the empirical relations of [Torres et al. \(2010\)](#), giving $M = 1.14 \pm 0.07 M_{\odot}$.

3. MODELING

Below we use the observational constraints from Section 2 to infer additional characteristics of 31 Aql from stellar modeling. In Section 3.1 we determine precise stellar properties from asteroseismic modeling. In Section 3.2 we estimate the wind braking torque from the prescription of [Finley & Matt \(2018\)](#). Finally, in Section 3.3 we constrain the angular momentum history from rotational evolution modeling.

3.1. Asteroseismology

Using the oscillation frequencies identified in Table 1, spectroscopic parameters from [Brewer et al. \(2016\)](#), and the luminosity constraint from Section 2.6, five teams inferred the properties of 31 Aql from asteroseismic modeling. A variety of stellar evolution codes and fitting methods were used, including ASTEC / AMP 1.3 ([Christensen-Dalsgaard 2008](#); [Metcalf et al. 2009](#); [Creevey et al. 2017](#)), GARSTEC / BASTA ([Aguirre Børsen-Koch et al. 2022](#)), MESA / AMP 2.0 ([Paxton et al. 2015](#); [Metcalf et al. 2023a](#)), and YREC ([Demarque et al. 2008](#)). We found reasonable agreement between the results for the asteroseismic properties, with individual estimates ranging from $R = 1.341$ –

Table 5. Adopted Properties of the Subgiant 31 Aql

	31 Aql	Source
T_{eff} (K)	5587 ± 78	1
$[M/H]$ (dex)	$+0.32 \pm 0.07$	1
$\log g$ (dex)	4.15 ± 0.08	1
$v \sin i$ (km s $^{-1}$)	1.3 ± 0.5	1
$B - V$ (mag)	0.77	2
$\log R'_{\text{HK}}$ (dex)	−5.099	2
$ B_d $ (G)	8.5 ± 1.1	3
L_X ($10^{27} \text{ erg s}^{-1}$)	2.4 ± 0.3	4
Mass-loss rate (\dot{M}_{\odot})	$1.05^{+1.08}_{-0.58}$	4
P_{rot} (days)	40.3 ± 1.5	5
Luminosity (L_{\odot})	1.557 ± 0.055	6
Radius (R_{\odot})	1.358 ± 0.016	7
Mass (M_{\odot})	1.07 ± 0.04	7
Age (Gyr)	8.9 ± 1.3	7
Torque (10^{30} erg)	$3.22^{+2.52}_{-1.53}$	8

References—(1) [Brewer et al. \(2016\)](#); (2) [Baliunas et al. \(1996\)](#); (3) Section 2.2; (4) Section 2.3; (5) Section 2.5; (6) Section 2.6; (7) Section 3.1; (8) Section 3.2

1.397 R_{\odot} , $M = 1.02$ – $1.15 M_{\odot}$, and stellar ages between 8.3–10.1 Gyr. We adopt the values and uncertainties from the AMP 2.0 pipeline, which yielded stellar properties that are most representative of the ensemble of results and produced an optimal reference model with a reduced $\chi^2 \sim 1$. The adopted properties for 31 Aql are summarized in Table 5.

The AMP 2.0 pipeline ([Metcalf et al. 2023a](#)) uses a parallel genetic algorithm ([Metcalf & Charbonneau 2003](#)) to optimize the match between the observational constraints and stellar models produced by version r12778 of the MESA stellar evolution code ([Paxton et al. 2015](#)) and version 6 of the GYRE pulsation code ([Townsend & Teitler 2013](#)). The stellar models use the default MESA equation of state, which is primarily from OPAL ([Rogers & Nayfonov 2002](#)) and SCVH ([Saumon et al. 1995](#)), OPAL opacities supplemented with low-temperature values from [Ferguson et al. \(2005\)](#), the [Grevesse & Sauval \(1998\)](#) solar mixture, NACRE nuclear reaction rates ([Angulo et al. 1999](#)), a gray atmosphere with [Eddington \(1926\) \$T\$ - \$\tau\$ integration, the mixing-length formalism of \[Cox & Giuli \\(1968\\)\]\(#\), diffusion and settling of helium and heavy elements from \[Thoul et al. \\(1994\\)\]\(#\), and the two term \[Ball & Gizon \\(2014\\) prescription for the asteroseismic surface correction. The values and uncertainties of the asteroseismic properties were determined from the likelihood-weighted mean and standard deviation of all models sampled by the genetic algorithm during the optimization.\]\(#\)](#)

3.2. Magnetic Evolution

We can now estimate the current wind braking torque for 31 Aql using the prescription of [Finley & Matt \(2018\)](#). Combining the large-scale magnetic field strength derived from spectropolarimetry in Section 2.2, the mass-loss rate inferred from the X-ray surface flux in Section 2.3, the mean rotation period from the chromospheric activity data in Section 2.5, and the precise stellar mass and radius from asteroseismology in Section 3.1, our wind braking torque estimate is $3.22^{+2.52}_{-1.53} \times 10^{30}$ erg. The dominant contributions to the total torque uncertainty (+78%, -48%) come from the errors on the estimated mass-loss rate (+47%, -35%) and the dipole field strength ($\pm 12\%$), followed by smaller contributions from the rotation period ($\pm 4\%$), the stellar radius ($\pm 4\%$), and the stellar mass ($\pm 1\%$).

The wind braking torque for 31 Aql is nearly an order of magnitude stronger than that of the younger solar analog 16 Cyg A (cf. [Metcalf et al. 2022](#)). The two stars have nearly the same mass and chromospheric activity, but 31 Aql has a lower surface gravity, larger radius, and slightly higher luminosity than 16 Cyg A, as well as an asteroseismic age that is about 1.5 Gyr older. Despite the difference in metallicity, if we treat these two stars as an evolutionary sequence we can investigate the sources of the large difference in their wind braking torques by changing one parameter at a time between the fiducial models for each star. We find that the large increase in the wind braking torque in this age range (7.4–8.9 Gyr) is driven primarily by the much stronger dipole field (+1240%), along with the slightly larger radius (+39%) and higher mass-loss rate (+7%) of 31 Aql, offset by the substantially longer rotation period (-49%).

Considering the simulation results of [Noraz et al. \(2024\)](#), it’s possible that 31 Aql may have reached the higher Ro regime where DR is predicted to shift from solar-like (fast equator, slow poles) to anti-solar (slow equator, fast poles). This transition apparently leads to a restoration of the large-scale magnetic field on the subgiant branch, after a prolonged phase of WMB during the second half of the main-sequence lifetime. Unlike the large-scale fields of younger main-sequence stars, the field produced by anti-solar DR in the simulations is stationary rather than cycling—in agreement with the flat activity record shown in Figure 4. We hypothesize that the restoration of the large-scale magnetic field with the transition to anti-solar DR produces a phase of revived magnetic braking on the subgiant branch. We explore this scenario using a toy model in the following section.

3.3. Rotational Evolution

If we model 31 Aql with assumptions identical to those in [Metcalf et al. \(2025\)](#) but including an asteroseismic prior on the stellar age (a Gaussian centered at 8.9 Gyr with $\sigma = 1.3$ Gyr), we predict a rotation period $P_{\text{rot}} = 33 \pm 4$ days

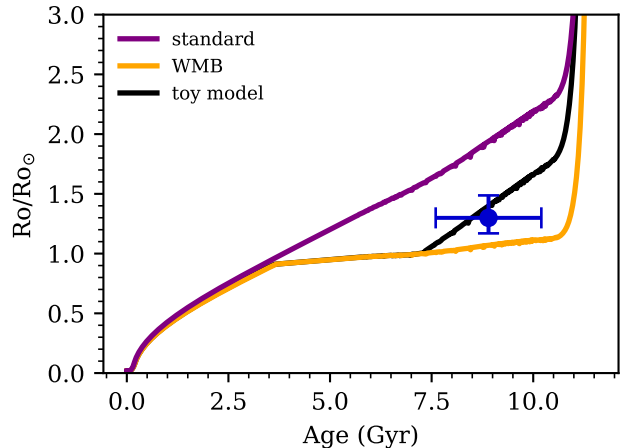


Figure 5. Rossby number as a function of time for a standard spin-down model (purple), WMB model (orange), and a toy model in which braking ceases at Ro_{crit} and resumes at Ro_{flip} (black). The standard and WMB cases are the median posterior tracks for models constrained to match the surface temperature, radius, and metallicity with an informative asteroseismic age prior. The black curve adds the parameter Ro_{flip} by including the observed rotation period as a constraint on the model.

under WMB, and $P_{\text{rot}} = 58 \pm 9$ days under a standard spin-down scenario—both in mild tension with the observed rotation period. 31 Aql appears to be a contradiction: it has an observed instantaneous torque consistent with standard braking, but it cannot have undergone that level of spin-down for its entire life and still retain its relatively rapid rotation. The simulations of [Noraz et al. \(2024\)](#) suggest a possible means to reconcile these observations: the establishment of anti-solar DR may eventually restore the torque.

To examine this scenario, we construct a toy model that incorporates a phase of WMB that begins at Ro_{crit} , with revived magnetic braking at a higher Ro where DR flips from solar-like to anti-solar (Ro_{flip}). In this toy model, both transitions are abrupt: angular momentum loss is set to zero at Ro_{crit} , and set to the standard braking after Ro_{flip} , given the instantaneous rotation period and stellar structure. In between these two transitions, the rotational evolution is dictated solely by the evolving moment of inertia as the star gradually expands on the main-sequence. Despite the lack of a wind braking torque, Ro slowly increases with time during this phase (see the orange line in Figure 5).

We fit for a value of Ro_{flip} using the following procedure. We fix the values of Ro_{crit} and the braking normalization (f_k) to those determined in [Saunders et al. \(2024\)](#) for WMB, but we leave Ro_{flip} as a free parameter (along with the model mass, metallicity, age, and mixing length). The prior on Ro_{flip} is uninformative aside from two limits: we require that $Ro_{\text{flip}} > Ro_{\text{crit}}$ and that the stellar age at Ro_{flip} is less than the

current age, which effectively incorporates a prior from the observed wind braking torque for 31 Aql.

We include the rotation period as a constraint on the model, adopting the value from Section 2.5 with an additional 10% error on the period, added in quadrature, to account for systematic uncertainty in the observed active latitudes (i.e. Epstein & Pinsonneault 2014). As in Metcalfe et al. (2025), the observed T_{eff} , $[M/H]$, and radius are used as constraints on the model, with values and errors adopted from Table 5, along with additional systematic uncertainties added in quadrature.

We find $\text{Ro}_{\text{flip}} = 1.1 \pm 0.05 \text{Ro}_{\text{crit}}$. Because the evolution between Ro_{crit} and Ro_{flip} is driven by slow structural changes to the star over a nuclear timescale, there is a sizable delay before the star reaches Ro_{flip} —in our model for 31 Aql, braking resumes $3.5^{+1.3}_{-2.2}$ Gyr after the onset of WMB, at an age of $7.1^{+1.6}_{-2.5}$ Gyr. This long pause in spin-down means that our toy model preserves many of the broad features of the original WMB model: stars undergo a prolonged phase of subdued spin-down during the latter half of the main-sequence, and thus a sizable population of objects should be observed in the midst of WMB.

4. DISCUSSION

The estimated wind braking torque and current Ro of 31 Aql appear to constrain the transition from solar-like to anti-solar DR in subgiant stars. In Figure 6 we reproduce the evidence from Metcalfe et al. (2025) for the gradual onset of WMB in older main-sequence stars, to which we add the new constraint from the G7 subgiant 31 Aql (labeled orange point). The efficiency of magnetic braking decreases by up to two orders of magnitude as stars approach Ro_{crit} slightly above the solar value. To explain the current wind braking torque and rotation period of 31 Aql, we find that standard magnetic braking may resume near $1.1 \text{Ro}_{\text{crit}}$ —apparently from a restoration of the large-scale magnetic field due to a shift of the DR pattern from solar-like to anti-solar, as suggested by recent simulations (Noraz et al. 2024).

Although we cannot directly constrain the sense of the DR from the chromospheric activity data, the observations reveal a variety of rotation periods in different seasons and minimal long-term variability on cycle timescales, consistent with the simulations. Previous support for the simulation results came from observations of enhanced photometric variability in Kepler targets at Ro above the solar value (Mathur et al. 2025), but 31 Aql suggests that the transition to anti-solar DR might be accompanied by a rejuvenation of the large-scale magnetic field and revived magnetic braking.

The revived magnetic braking due to anti-solar DR is distinct from the born-again dynamo phenomenon discovered in 94 Aqr Aa (Metcalfe et al. 2020) and confirmed in β Hyi (Metcalfe et al. 2024; Santos et al. 2025). The latter occurs in stars with shallower convective envelopes, when physical

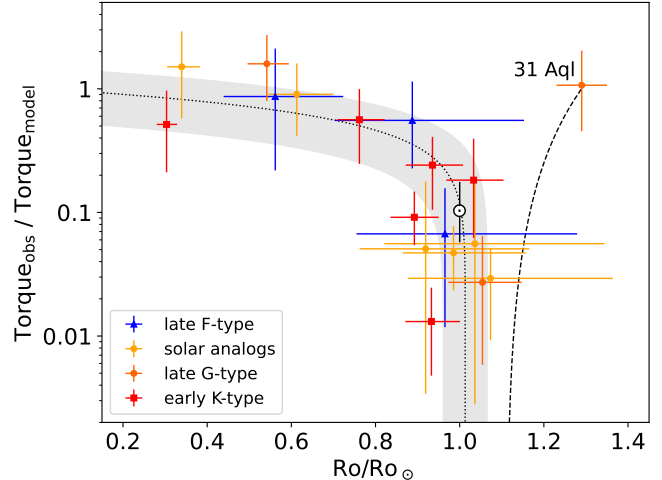


Figure 6. Ratio of the observationally estimated and model wind braking torque as a function of Rossby number normalized to the solar value. The dotted line and gray shaded region illustrates the fit and 95% confidence interval described by Metcalfe et al. (2025). The revived magnetic braking in 31 Aql at higher Ro is evident, and quadratic growth is illustrated schematically with a dashed line.

expansion on the subgiant branch initially pushes Ro above Ro_{crit} , leading to a collapse of the global dynamo. However, subsequent structural evolution pushes Ro back below Ro_{crit} , reinvigorating the dynamo near the base of the red giant branch. Stars with deeper convection zones like 31 Aql do not experience this “blue hook”, but instead show a steadily increasing Ro along the subgiant branch. This steady evolution leads to a collapse of the global dynamo when Ro exceeds Ro_{crit} , followed by revived magnetic braking when Ro exceeds Ro_{flip} and a non-cycling large-scale magnetic field is produced. Despite these distinct trajectories, it is possible that stars with born-again dynamos might have exceeded Ro_{flip} somewhere along their evolutionary paths, which may provide complementary constraints on Ro_{flip} .

A more sophisticated treatment of the rotational evolution would incorporate the gradual onset of WMB as Ro approaches Ro_{crit} and the gradual resumption of magnetic braking above Ro_{flip} . Our toy model is a step function that eliminates magnetic braking at Ro_{crit} and another step function that resumes magnetic braking at Ro_{flip} . The functional form of the gradual onset shown in Figure 6 is a generic prediction of a Hopf bifurcation, with the dynamo efficiency decreasing as $\sqrt{\text{Ro}_{\text{crit}} - \text{Ro}}$ (Cameron & Schüssler 2017). This treatment is appropriate for the transition from an oscillatory to a stationary solution, while the shift from solar-like to anti-solar DR in a non-oscillatory dynamo can be described by a transcritical bifurcation with a quadratic growth in dynamo efficiency at $\text{Ro} > \text{Ro}_{\text{flip}}$ (dashed line in Figure 6). A refined analysis that replaces the step functions in our toy model with the expected functional forms for these two transitions could

improve our estimate of the absolute value of Ro (not just relative to Ro_{crit}) where DR shifts from solar-like to anti-solar.

The simulations described by Brun et al. (2022) and analyzed by Noraz et al. (2024) were not designed to probe evolution beyond the main-sequence, so their constraints on Ro_{flip} may not be entirely correct for a subgiant. Although the authors noted the expected influence of WMB, the simulations attempted to follow the evolution of main-sequence stars under a scenario of standard magnetic braking. As such, the background stellar structure in the simulations at Ro above the solar value was appropriate for evolved main-sequence stars rather than subgiants. The limited sampling of Ro in these computationally expensive simulations currently suggests the existence of Ro_{flip} somewhere between $0.76\text{--}1.38 Ro_{\odot}$ (see Fig.1 in Noraz et al. 2024). Future simulations in this range of Ro with a background stellar structure appropriate for subgiant stars may provide stronger constraints on the estimated value of Ro_{flip} .

The inclination of 31 Aql ($i \sim 61^\circ$) is favorable for the asteroseismic detection of rotational splittings that could distinguish between solar-like and anti-solar DR. In particular, the visibility of both the inner ($m = \pm 1$) and outer ($m = \pm 2$) splittings for an $\ell = 2$ quintuplet is optimal at $i = 60^\circ$ (Gizon & Solanki 2003). The latter ($\ell = m$) probe the equatorial rotation rate while the former ($\ell \neq m$) probe the rotation at higher latitudes (Davies et al. 2015), so the relative splittings can reveal the sense of the DR. This technique has already been demonstrated for several dozen Kepler targets (Benomar et al. 2018; Bazot et al. 2019), requiring long-term high S/N observations. Such measurements may be possible from a careful analysis of KIC 8349582 (Kepler-95), a close analog of 31 Aql in the Kepler field of view. The duration of

TESS observations is currently too limited to resolve rotational splittings, and the proposed PLATO fields do not include 31 Aql (Nascimbeni et al. 2022). However, the higher S/N of ground-based radial velocity observations for asteroseismology should be able to resolve the rotational splittings and decipher between solar-like and anti-solar DR in 31 Aql. Future multi-month monitoring by the Stellar Observations Network Group (SONG; Grundahl et al. 2008) might provide the necessary S/N for such a measurement.

T.S.M. acknowledges support from Chandra award GO0-21005X, NSF grant AST-2205919, and TESS General Investigator grant 80NSSC25K7898. Computational time at the Texas Advanced Computing Center was provided through ACCESS allocation TG-AST090107. J.v.S. acknowledges support from NSF grant AST-2205888. D.B. acknowledges support from TESS General Investigator grant 80NSSC19K0385. R.A.G. acknowledges support from the GOLF and PLATO Centre National D'Études Spatiales (CNES) grant. O.K. acknowledges support from the Swedish Research Council (grant agreement no. 2023-03667) and the Swedish National Space Agency. S.H.S. is grateful for support from award HST-GO-15991.002-A. A.S. acknowledges support from the European Research Council (ERC) under the European Union's Horizon 2020 research and innovation program (CartographyY; grant agreement 804752). T.R.B. is supported by the Australian Research Council (FL220100117). S.N.B. acknowledges support from PLATO ASI-INAF agreement no. 2022-28-HH.0 "PLATO Fase D". The TESS and HST data used in this paper can be found on MAST: <https://doi.org/10.17909/0vak-d288>.

REFERENCES

- Aguirre Børsen-Koch, V., Rørsted, J. L., Justesen, A. B., et al. 2022, *MNRAS*, 509, 4344
- Angulo, C., Arnould, M., Rayet, M., et al. 1999, *NuPhA*, 656, 3
- Ayres, T. 2025, *AJ*, 169, 281
- Ayres, T. R. 2020, *ApJS*, 250, 16
- Baliunas, S., Sokoloff, D., & Soon, W. 1996, *ApJL*, 457, L99
- Baliunas, S. L., Donahue, R. A., Soon, W. H., et al. 1995, *ApJ*, 438, 269
- Ball, W. H., & Gizon, L. 2014, *A&A*, 568, A123
- Baum, A. C., Wright, J. T., Luhn, J. K., & Isaacson, H. 2022, *AJ*, 163, 183
- Bazot, M., Benomar, O., Christensen-Dalsgaard, J., et al. 2019, *A&A*, 623, A125
- Benomar, O., Bazot, M., Nielsen, M. B., et al. 2018, *Science*, 361, 1231
- Bowler, B. P., Tran, Q. H., Zhang, Z., et al. 2023, *AJ*, 165, 164
- Breton, S. N., García, R. A., Ballot, J., Delsanti, V., & Salabert, D. 2022, *A&A*, 663, A118
- Brewer, J. M., Fischer, D. A., Valenti, J. A., & Piskunov, N. 2016, *ApJS*, 225, 32
- Brun, A. S., Strugarek, A., Noraz, Q., et al. 2022, *ApJ*, 926, 21
- Cameron, R. H., & Schüssler, M. 2017, *ApJ*, 843, 111
- Christensen-Dalsgaard, J. 2008, *Ap&SS*, 316, 13
- Cox, J. P., & Giuli, R. T. 1968, Principles of stellar structure (Gordon and Breach, New York)
- Creevey, O. L., Metcalfe, T. S., Schultheis, M., et al. 2017, *A&A*, 601, A67
- Davies, G. R., Chaplin, W. J., Farr, W. M., et al. 2015, *MNRAS*, 446, 2959
- Demarque, P., Guenther, D. B., Li, L. H., Mazumdar, A., & Straka, C. W. 2008, *Ap&SS*, 316, 31
- Donahue, R. A. 1993, PhD thesis, New Mexico State University

- Donahue, R. A., Saar, S. H., & Baliunas, S. L. 1996, *ApJ*, 466, 384
- Donati, J. F., Semel, M., Carter, B. D., Rees, D. E., & Collier Cameron, A. 1997, *MNRAS*, 291, 658
- Eddington, A. S. 1926, *The Internal Constitution of the Stars* (Cambridge: Cambridge University Press)
- Epstein, C. R., & Pinsonneault, M. H. 2014, *ApJ*, 780, 159
- Ferguson, J. W., Alexander, D. R., Allard, F., et al. 2005, *ApJ*, 623, 585
- Finley, A. J., & Matt, S. P. 2018, *ApJ*, 854, 78
- Fletcher, S. T., Chaplin, W. J., Elsworth, Y., & New, R. 2008, *AN*, 329, 447
- Foreman-Mackey, D., Hogg, D. W., Lang, D., & Goodman, J. 2013, *PASP*, 125, 306
- García, R. A., Mathur, S., Pires, S., et al. 2014, *A&A*, 568, A10
- Gastine, T., Yadav, R. K., Morin, J., Reiniers, A., & Wicht, J. 2014, *MNRAS*, 438, L76
- Gizon, L., & Solanki, S. K. 2003, *ApJ*, 589, 1009
- Grevesse, N., & Sauval, A. J. 1998, *SSRv*, 85, 161
- Grundahl, F., Christensen-Dalsgaard, J., Arentoft, T., et al. 2008, *CoAst*, 157, 273
- Huber, D., White, T. R., Metcalfe, T. S., et al. 2022, *AJ*, 163, 79
- Jenkins, J. M., Twicken, J. D., McCauliff, S., et al. 2016, *Proc. SPIE*, 9913, 99133E
- Judge, P. G., Kleint, L., Leenaarts, J., Sukhorukov, A. V., & Vial, J.-C. 2020, *ApJ*, 901, 32
- Keenan, F. P., Dufton, P. L., Aggarwal, K. M., & Kingston, A. E. 1988, *ApJ*, 324, 1068
- Keenan, F. P., Kingston, A. E., & Dufton, P. L. 1987, *MNRAS*, 225, 859
- Kochukhov, O., Makaganiuk, V., & Piskunov, N. 2010, *A&A*, 524, A5
- Mathur, S., Santos, Á. R. G., Claytor, Z. R., et al. 2025, *ApJ*, 982, 114
- Mermilliod, J. C. 2006, *VizieR Online Data Catalog*, II/168
- Metcalfe, T. S., & Charbonneau, P. 2003, *JCoPh*, 185, 176
- Metcalfe, T. S., Creevey, O. L., & Christensen-Dalsgaard, J. 2009, *ApJ*, 699, 373
- Metcalfe, T. S., Egeland, R., & van Saders, J. 2016, *ApJL*, 826, L2
- Metcalfe, T. S., Kochukhov, O., Ilyin, I. V., et al. 2019, *ApJL*, 887, L38
- Metcalfe, T. S., Townsend, R. H. D., & Ball, W. H. 2023a, *RNAAS*, 7, 164
- Metcalfe, T. S., & van Saders, J. 2017, *SoPh*, 292, 126
- Metcalfe, T. S., van Saders, J. L., Basu, S., et al. 2020, *ApJ*, 900, 154
- Metcalfe, T. S., Finley, A. J., Kochukhov, O., et al. 2022, *ApJL*, 933, L17
- Metcalfe, T. S., Buzasi, D., Huber, D., et al. 2023b, *AJ*, 166, 167
- Metcalfe, T. S., van Saders, J. L., Huber, D., et al. 2024, *ApJ*, 974, 31
- Metcalfe, T. S., van Saders, J. L., Pinsonneault, M. H., et al. 2025, *ApJL*, 991, L17
- Nascimbeni, V., Piotto, G., Börner, A., et al. 2022, *A&A*, 658, A31
- Nielsen, M. B., Ball, W. H., Standing, M. R., et al. 2020, *A&A*, 641, A25
- Noraz, Q., Brun, A. S., & Strugarek, A. 2024, *A&A*, 684, A156
- Paunzen, E. 2015, *A&A*, 580, A23
- Paxton, B., Marchant, P., Schwab, J., et al. 2015, *ApJS*, 220, 15
- Petit, P., Louge, T., Théado, S., et al. 2014, *PASP*, 126, 469
- Pires, S., Mathur, S., García, R. A., et al. 2015, *A&A*, 574, A18
- Proudman, J. 1916, *RSPSA*, 92, 408
- Rao, Y. K., Del Zanna, G., Mason, H. E., & Dufresne, R. 2022, *MNRAS*, 517, 1422
- Ricker, G. R., Winn, J. N., Vanderspek, R., et al. 2014, *Proc. SPIE*, 9143, 914320
- Roca Cortés, T., Jiménez, A., Pallé, P. L., GOLF team, & VIRGO Team. 1999, *ESA SP*, 448, 135
- Rogers, F. J., & Nayfonov, A. 2002, *ApJ*, 576, 1064
- Ryabchikova, T., Piskunov, N., Kurucz, R. L., et al. 2015, *PhyS*, 90, 054005
- Santos, A. R. G., Metcalfe, T. S., Kochukhov, O., et al. 2025, *A&A*, 698, L23
- Saumon, D., Chabrier, G., & van Horn, H. M. 1995, *ApJS*, 99, 713
- Saunders, N., van Saders, J. L., Lyttle, A. J., et al. 2024, *ApJ*, 962, 138
- Skumanich, A. 1972, *ApJ*, 171, 565
- Stassun, K. G., Collins, K. A., & Gaudi, B. S. 2017, *AJ*, 153, 136
- Stassun, K. G., Corsaro, E., Pepper, J. A., & Gaudi, B. S. 2018, *AJ*, 155, 22
- Stassun, K. G., & Torres, G. 2016, *ApJL*, 831, L6
- , 2021, *ApJL*, 907, L33
- Strassmeier, K. G., Ilyin, I., Järvinen, A., et al. 2015, *AN*, 336, 324
- Strugarek, A., Beaudoin, P., Charbonneau, P., Brun, A. S., & do Nascimento, J.-D. 2017, *Science*, 357, 185
- Taylor, G. I. 1917, *RSPSA*, 93, 99
- Thompson, M. J., Toomre, J., Anderson, E. R., et al. 1996, *Science*, 272, 1300
- Thoul, A. A., Bahcall, J. N., & Loeb, A. 1994, *ApJ*, 421, 828
- Torres, G., Andersen, J., & Giménez, A. 2010, *A&A Rv*, 18, 67
- Townsend, R. H. D., & Teitler, S. A. 2013, *MNRAS*, 435, 3406
- van Saders, J. L., Ceillier, T., Metcalfe, T. S., et al. 2016, *Nature*, 529, 181
- Vaughan, A. H., Preston, G. W., & Wilson, O. C. 1978, *PASP*, 90, 267
- Weber, M., Strassmeier, K. G., & Washuettl, A. 2005, *AN*, 326, 287
- Wilson, O. C. 1978, *ApJ*, 226, 379
- Wood, B. E. 2018, *JPhCS*, 1100, 012028
- Wood, B. E., Müller, H. R., Zank, G. P., Linsky, J. L., & Redfield, S. 2005, *ApJL*, 628, L143